On the dynamic assessment of the Local-Maximum Entropy Material Point Method through an Explicit Predictor-Corrector Scheme

Miguel Molinos, Pedro Navas, Manuel Pastor and Miguel Martín-Stickle.

Highlights

- We have proposed a new and efficient time integration scheme for the MPM in order to dissipate spurious stress oscillations without damping the solution.

- The proposal of the LME approximation technique under the MPM framework is a robust substitute of the traditional shape functions.

- Our approach have clear benefits on large strain fast dynamic simulations, where the grid-crossing pathology appears.

On the dynamic assessment of the Local-Maximum Entropy Material Point Method through an Explicit Predictor-Corrector Scheme

Miguel Molinos[a], Pedro Navas[a1], Manuel Pastor[a] and Miguel Martín Stickle[a]

[a] *ETSI Caminos, Canales y Puertos, Universidad Politéctnica de Madrid. c. Prof. Aranguren 3, 28040 Madrid, Spain*

Abstract

Material Point Method (MPM) has arisen in the recent years as an alternative to Finite Element Method (FEM) under the large deformation regime. However, the simulation of shock waves propagation in the large deformation regime is still challenging under this approach due the incapability of the standard MPM time integration scheme to filter spurious noises. To overcome it, we propose in this paper an explicit Predictor-Corrector time integration scheme. Its powerful performance mitigates the presence of spurious oscillations with minimal dissipation in high frequency problems. Other source of numerical noise in MPM occurs when the material points cross computational grid boundaries, being caused by the lack of smoothness of the interpolation functions. This noise results in spurious local variations at the material points, where strain-stress fields are computed. This could lead to inaccurate solutions as well as aborted simulations in the worst cases. To surmount it, we propose in this work the Local Maximum-Entropy (LME) approximation schemes as a robust substitute of the traditional shape function in MPM. LME approximation may be regarded as a *thermalization* of Delaunay triangulation which resolves the degenerate cases resulting from the lack or uniqueness of the triangulation. Furthermore, by modifying a regularization parameter, they are able to behave finite element like or as a meshfree method. This capability allows to face a wide range of physics

---

[1]Corresponding author: p.navas@upm.es

with a single shape function family. Finally this paper demonstrates the performance of both improvements through numerical examples.

1. Introduction

Since the proposal of MPM by Sulsky *et al.* (1994) [1] as a generalization to solids of the Fluid Implicit Particle (FLIP) method [2], its popularity has increased due to its ability to deal with large strain regime without suffering ⁵ mesh distortion inaccuracies. One of the main fields where this method is strong is the solid dynamics since the original time integration scheme proposed was the Forward Euler (FE) [1], carried out in an explicit manner. However, in this type or problems, the main instabilities of the original MPM are even marked.

¹⁰ On the one hand, the main source of instability occurs when material points cross cell boundaries. This provoked the development of other interpolation techniques to overcome this limitation such as the Generalized Interpolation Material Point (GIMP) method Bardenhagen & Kober (2004) [3], which has demonstrated to have a good performance in the finite defor- ¹⁵ mation regime. However, in the absence of a regular grid, construction of the weighting functions is only achieved at considerable effort and computational cost. Furthermore, as it is a voxel-based discretisation technique, it is prone to suffer voxel domains overlap or gaps when the material point mesh becomes irregular, which can introduce severe inaccuracies as noticed ²⁰ by Steffen *et al.* (2008)[4]. This is similar to the difficulty encountered by the finite element methods due to element distortion. A more robust alternative is the Dual Domain Material Point (DDMP) method proposed by Zhang *et al.* (2011) [5]. Unfortunately this method shows an unsatisfactory behaviour when particle/cell ratio decreases. Therefore DDMP a large number of par- ²⁵ ticles is needed for convergence [6], what makes the method very expensive. To avoid the tensile instabilities quite commons in extensions, Sadeghirad *et al.* (2011) [7] developed the CPDI [7] . In recent years the employment of spline-lines as shape functions has gain popularity with the introduction of the B-Spline MPM proposed by Tielen *et al.* (2017) [8], this technique ³⁰ allows the employment of unstructured set of notes and particles. More recently, approximants derived from minimization has been introduced in to the MPM framework with the Conservative Taylor Least Squares (CTLS) reconstruction proposed by Wobbes *et al.* (2018) [9]. Unfortunately, when particles are spread in some particular special patterns, the quality of the ³⁵ CTLS approximation decreases locally.

This document adopts the Local Maximum-Entropy (LME), or Local *Max-Ent* approximates, as a robust substitute of the aforementioned shape functions in MPM. First introduced by Arroyo & Ortiz (2006) [10], it belongs to the class of convex approximation schemes and provides a seamless transition between FEM and meshfree interpolations. The approximation scheme is based on a compromise between minimizing the width of the shape function support and maximizing the information entropy of the approximation. The LME approximation may be regarded as a regularization, or *thermalization*, of Delaunay triangulation which effectively resolves the degenerate cases resulting from the lack of uniqueness or the triangulation. LME basis functions possess many desirable properties for meshfree algorithms. First of all, they are entirely defined by the nodal set and the domain of analysis. They are also non-negative, satisfy the partition of unity property, and provide an exact approximation for related functions [10]. Important contributions on the Maximum-Entropy have been made by Sukumar and coworkers [11] with Cell-based techniques and the ones carried within the Optimal Transportation Meshfree (OTM) method. The latter methodology has been proven to have a good performance under the dynamic regime by other researchers, being important the contributions of Li *et al.* (2012) [12] and Navas *et al.* (2018) [13, 14] in the explicit regime and Navas *et al.* [15, 16, 17] and Wriggers and coworkers [18] with implicit schemes. More recently, under MPM framework, the work made by Wobbes *et al.*(2020) [19]. The proposed research delves into the benefits of the regularization parameter, β, and the analogy of the different obtained shape functions derive by the tuning of this parameter and the traditional MPM ones.

The aforementioned techniques are devoted to mitigate the "grid crossing" error. Nevertheless, in the presence of shock waves spurious, numerical noises appear despite of the employment of these techniques [20]. These numerical inaccuracies, also known as wiggles, arise due to inaccuracies in the time discretisation technique. A simple approach to face those spurious noises lies on the addition of nonphysical damping sources to the equilibrium equations. This approach has been widely employed in this and many other numerical techniques. To avoid introducing this nonphysical sources, many researchers have proposed alternative time integration schemes which reduce the presence of high frequency noises by filtering them or increasing somehow the accuracy. One of the first attempts was the proposal of an implicit time integration scheme by Guilkey & Weiss [21]. More recently Wang *et al.* [22] mitigated these spurious noises by adding a non-viscous damping to the linear momentum balance equation, and later Charlton *et al.* [23] extended this scheme to the GIMP approach introducing the Implicit GIMP (iGIMP) method. However, the local damping introduced by [22] can totally

4

over-damp the solution in time-dependent simulations such as in consolidation process. In a recent publication, Kularathna & Soga [24] studied an implicit treatment of the pressure in MPM algorithm to simulate material incompressibility avoiding artificial pressure oscillations by applying Chorin's projection. Within the explicit time integration schemes, Lu *et al.*[25] introduced the time-discontinuous Galerkin method to control the spurious noises propagation, and later Tran & Solowski [20] proposed a generalised-α scheme for MPM with promising results but at the expense of increasing the computational effort. In this paper a less time consuming and high efficient explicit predictor-corrector integration method is proposed. It consists of an accommodation of the traditional Newmark Predictor-Corrector (NPC) scheme, widely employed in Finite Element methods. This method has been chosen among other suitable alternatives as those proposed by Wilson *et al.* (1972) [26] or Chung & Hulbert (1993) [27] because its simplicity and good performance dealing with solid dynamic problems under a meshfree framework in [14].

The aim of this document is to mitigate the spurious oscillations due to inaccuracies in both space and time discretisation by the employment of a suitable combination of the LME family shape functions, and the proposal of an explicit predictor-corrector scheme. The advantages of this approach will be illustrated through several demanding test cases on the elastic regime: the propagation of shock waves in an elastic bar and the response of a block of soil gradually loaded with gravitational forces.

The article is organised as follows. Section 2 is devoted to describe the meshfree methodology adopted in this research, first MPM procedure is introduced in 2.1, second the explicit predictor-corrector time integration scheme is presented in 2.2, and third LME approximation scheme will be introduced in 2.3. In Section 3 applications to prove the numerical accuracy of the proposed approach are presented. Finally, conclusions and future research topics are exposed in Section 4.

2. The meshfree methodology

The aim of this section is to provide an overview of the standard explicit MPM algorithm [1]. Without loosing generality, the method consists of three main steps: (i) a variational recovery process, where particle data is projected onto the grid nodes, (ii) an Eulerian step, where balance of momentum equation is expressed as a nodal equilibrium equation through a FEM-like procedure, and finally (iii) a Lagrangian advection of the particles. In consequence, MPM can be regarded as a Lagrangian-Eulerian method where particles carry on all the physical information and a set of background
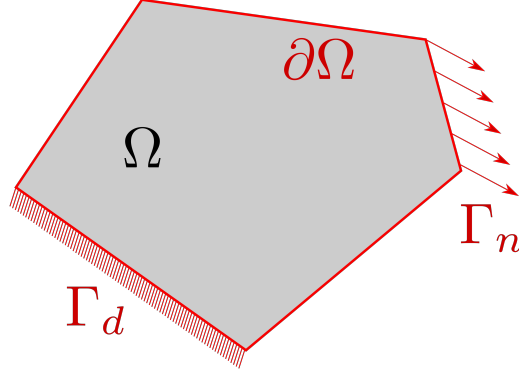
5

Figure 1: Description of the boundary-value-problem in a continuum. Red lines represents the closure $\partial\Omega$ of the domain Ω represented in gray.

nodes is employed to compute the equilibrium equation. In what follows, we will adopt the following convention. Three kind of subscripts or superscripts are used within paper. The subscript $\square_p$ is used to define a particle variable. While the subscript $\square_I$ is reserved in this notation for denoting nodal variables. And finally, the superscript $\square^\psi$ involves a virtual magnitude. For the operators, the convention is: $\dot{\square}$ and $\ddot{\square}$ for the first and second time derivative, $\square \otimes \square$ means the dyadic operator, $\square \cdot \square$ and $\square : \square$ means the first and second contraction of a tensor, $div(\square)$ denotes the divergence operator, and finally $grad(\square)$ and $grad^s(\square)$ denotes the gradient and its symmetric part. Einstein subscripts convention is adopted therefore repeated index means addition. Following, the MPM methodology, the explicit predictor-corrector scheme and LME approximation shape functions are describe in subsection 2.1,2.2 and 2.3 respectively.

2.1. Derivation of MPM procedure

In MPM the continuum mechanics approach is considered. So on, we will consider a region Ω occupied by an elastic body like the sketched in the figure 1, and $\partial\Omega$ the boundaries of the domain defined by $\partial\Omega = \Gamma_d \cup \Gamma_n$ and $\Gamma_d \cap \Gamma_n = \emptyset$. In this context the field $\vec{u}$ allows to describe the *global state* of the system. Now the variable $\phi = (\varepsilon, \sigma)$ is defined as the set of *local states* at any point of the continuum which can be derived from the field $\vec{u}$ through the following set of governing equations and restrictions that must be satisfied. First (i) we will relate global to local state by the *compatibility equation*, where the the strain field ε is extracted from $\vec{u}$ is defined as:

$$\varepsilon = grad^s(\vec{u}), \tag{1}$$

together with essential or Dirichlet boundary conditions (DBC) Γ_d. We will further assume that strains are infinitesimal, therefore second order terms in

the spatial derivatives can be neglected. From here, the stress field σ will be considered the corresponding conjugate variable for the strain field, being the one which satisfies (ii) the *conservation of lineal momentum equation*:

$$\rho \frac{D\vec{v}}{Dt} = div(\sigma) + \rho\vec{b} \tag{2}$$

together with the natural of Neumann boundary conditions (NBC) Γ_n. An aditional component will be (iii) the constitutive equation as a linear application from $\mathbb{R}^n$ to $\mathbb{R}^n$, which relate stress and strain increments as,

$$\sigma = \mathbf{D} : \varepsilon. \tag{3}$$

In this research, plane strain Linear Elasticity has been considered. Thus the constitutive tensor, $\mathbf{D}$, is the well known linear elastic one. The final equation of the set is (iv) the mass conservation, which can be obtained by setting to zero the total derivative of the density field,

$$\frac{D\rho}{Dt} = \dot{\rho} + \rho \, div(\vec{v}) = 0. \tag{4}$$

In order to obtain the variational statement of the problem, let us define a virtual displacement field such that

$$\vec{u}^{\psi} \in \mathcal{H}_0^1(\Omega) = \{\vec{u}^{\psi} \in \mathcal{H}^1 \mid \vec{u}^{\psi} = \vec{0} \text{ on } \Gamma_d\}; \tag{5}$$

in which the Cauchy sequences are convergent in Ω as well:

$$\int_{\Omega} \vec{u}^{\psi} \, d\Omega < \infty \quad \text{and} \quad \int_{\Omega} \varepsilon^{\psi} \, d\Omega < \infty. \tag{6}$$

The principle of virtual work states that the equilibrium solution to the boundary-value problem of elasticity is the function $\vec{u} \in \mathcal{H}_0^1$ such that, for any $\vec{u}^{\psi} \in \mathcal{H}_0^1$, the following holds:

$$\int_{\Omega} \rho \left(\frac{d\vec{v}}{dt} - \vec{b} \right) \cdot \vec{u}^{\psi} \, d\Omega = \int_{\Gamma_d} \vec{t} \cdot \vec{u}^{\psi} \, d\Gamma - \int_{\Omega} \sigma : \varepsilon^{\psi} \, d\Omega. \tag{7}$$

130

Thus, equation (7), together with (3) and (4), represents the weak form formulation of the problem. Next, we will discretise the set of equations of the mathematical model using a double discretisation procedure, see figure 2.

First, the velocity field and the virtual displacements fields are discretised in a finite set of nodes $\mathbf{X} = \{\vec{x}_I, I \in \mathcal{B}\} \subset \mathbb{R}^n$, where $\mathcal{B} = 1, \dots, N_I$. The

continuum field can be reconstructed with the help of nodal values and an appropriate interpolation function $N_I(\vec{x})$. Also spatial derivatives of those quantities, such as gradients and divergences, are computed through the support of the background set of nodes as.

$$\varphi(\vec{x}) = \sum_{I \in \mathcal{B}} N_I(\vec{x}) \, \varphi_I \tag{8}$$

$$grad(\varphi)(\vec{x}) = \sum_{I \in \mathcal{B}} grad(N_I(\vec{x})) \, \varphi_I \tag{9}$$

Secondly, the continuum Ω is discretised with a finite set of material points (also denominated particles the manuscript) $\hat{\Omega} = \{\vec{x}_p, p \in \mathcal{C}\} \subset \Omega$, where $\mathcal{C} = 1, \ldots, N_p$. Any particle field such as position, velocity, mass, volume and stress denoted by $\vec{x}_p$, $\vec{v}_p$, m_p, V_p and σ_p respectively are assigned to each material point. Furthermore, any particle field φ_p can be reconstructed within the nodes in the neighbourhood of each particle, $\mathcal{B}_p \subset \mathcal{B}$, and evaluating the interpolation function in the position of each particle as

$$\varphi_p = \sum_{I \in \mathcal{B}_p} N_I(\vec{x}_p) \, \varphi_I \tag{10}$$

$$grad(\varphi_p) = \sum_{I \in \mathcal{B}_p} grad(N_I(\vec{x}_p)) \, \varphi_I \tag{11}$$

Regarding numerical integration, the material derivatives are evaluated using the Riemann integral definition [28] applied to a finite set of points which associated volumes V_p are interpreted as quadrature weights.

$$\int_\Omega \varphi \, d\Omega = \sum_{p \in \mathcal{C}} \varphi_p \, V_p \tag{12}$$

Let us illustrate the procedure described above by fully developing the term of the acceleration forces in (7). Employing the definition (8) the velocity and virtual displacement fields can be approximated within its nodal values. Hence, the acceleration forces is reduced to

$$\sum_{I,J \in \mathcal{B}} \int_\Omega \rho \, N_J(\vec{x}) \frac{d\vec{v}_J}{dt} \cdot N_I(\vec{x}) \vec{u}_I^\psi \, d\Omega. \tag{13}$$

Rearranging terms in 13, and subtracting from the integral those discrete variables, the following expression is obtained

$$\sum_{I,J \in \mathcal{B}} \vec{u}_I^\psi \cdot \int_\Omega N_I(\vec{x}) \, \rho \, N_J(\vec{x}) \, d\Omega \, \frac{d\vec{v}_J}{dt}. \tag{14}$$
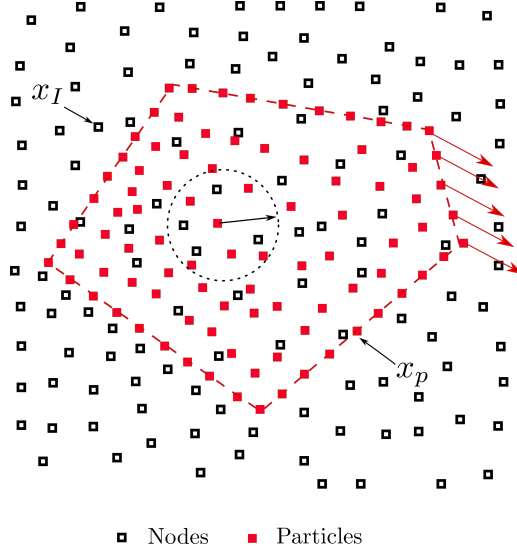
Figure 2: Description of the spatial discretisation for domain presented in the figure 1. Blue mesh represent the background computational support, and the red mesh conforms the discretised continuum body.

Now, employing the particle integral definition (12) to compute the integral of (14), and simplifying the it, is possible to achieve a discrete expression o the acceleration forces term as

$$
\sum_{I,J \in \mathcal{B}} \vec{u}_I^\psi \cdot \sum_{p \in \mathcal{C}} N_{Ip} \, \rho_p \, N_{Jp} \, V_p \, \frac{d\vec{v}_J}{dt} =
$$
$$
= \sum_{I,J \in \mathcal{B}} \vec{u}_I^\psi \cdot \sum_{p \in \mathcal{C}} N_{Ip} \, m_p \, N_{Jp} \, \frac{d\vec{v}_J}{dt} = \tag{15}
$$
$$
= \mathbf{m}_{IJ} \, \frac{d\vec{v}_J}{dt}
$$

Where $\mathbf{m}_{IJ}$, is the nodal mass matrix, and N_{Ip}, N_{Jp} are the interpolation functions for nodes I, J evaluated in the position of each particle p. In order to improve the computational efficiency and stability, the nodal mass matrix can be substituted by the lumped mass matrix $\mathbf{m}_{IJ}^{lumped}$. The remaining terms of (7) are obtained within a similar procedure and can be found in literature, see for instance [29]. So equation (7) has been discretised as

$$
\mathbf{m}_{IJ} \, \frac{d\vec{v}_J}{dt} = \sum_{p \in \mathcal{C}} -\sigma_p \cdot grad(N_{Ip})\frac{m_p}{\rho_p} + N_{Ip} \, \vec{b}_p \, m_p + N_{Ip} \, \vec{t}_p^s \, m_p h^{-1} \tag{16}
$$

Where h is the soil thickness in 2D, and $\sigma_p = \sigma_p(\varepsilon_p)$ is the particle p stress field, which can be integrated employing the suitable constitutive model. The

particle strain field is approximated thorough the time integration of the rate of stress tensor, which is computed employing the velocity at the background set of nodes by the equation

$$\dot{\varepsilon}_p = \frac{\Delta \varepsilon_p}{\Delta t} = \sum_{I \in \mathcal{B}_p} \frac{1}{2} \left[grad(N_{Ip}) \otimes \vec{v}_I + \vec{v}_I \otimes grad(N_{Ip}) \right]. \qquad (17)$$

Finally, mass conservation is guaranteed by enforcing the null value of the material derivative of the density field $\frac{D\rho}{Dt} = 0$. This leads to a suitable equation to update the density field:

$$\dot{\rho} = -\rho \ trace\left(\dot{\varepsilon}\right). \qquad (18)$$

Observe that to solve the equation (16), a second order time integration scheme is required. Therefore, time is discretised into a finite set of time steps $k = 1 \ldots, Nt$, where k is the current time step and N_t is the total number of time steps. Once the nodal equilibrium equation is solved, the values at the nodes are interpolated back into the particles, which are advected to the new position through:

$$\dot{\vec{v}}_p = \sum_{I \in \mathcal{B}_p} N_{Ip} \ \vec{a}_I, \quad \text{and} \quad \dot{\vec{x}}_p = \sum_{I \in \mathcal{B}_p} N_{Ip} \ \vec{v}_I. \qquad (19)$$

135   Traditionally, Eqs. (16) and (19), are solved with an explicit forward Euler algorithm. In the following subsection, this and the proposed schemes are described.

2.2. MPM time integration scheme: the Newmark Predictor-Corrector proposal

As was stated previosuly, an explicit forward Euler algorithm has been utilized widely within the MPM methodology. This scheme has been described in detail by many researchers [1], [30], [31] and can be sketched by the scheme of the figure 3. Other authors have proposed many others time integration alternatives like [21, 23, 20]. In the first publication on MPM [1], the nodal acceleration was employed to update the particles as

$$\vec{v}_p^{k+1} = \vec{v}_p^k + \sum_{I \in \mathcal{B}_p} \Delta t \ N_{Ip}^k \ \vec{a}_I^k, \qquad (20)$$

$$\vec{x}_p^{k+1} = \vec{x}_p^k + \sum_{I \in \mathcal{B}_p} \Delta t \ N_{Ip}^k \ \vec{v}_I^k. \qquad (21)$$
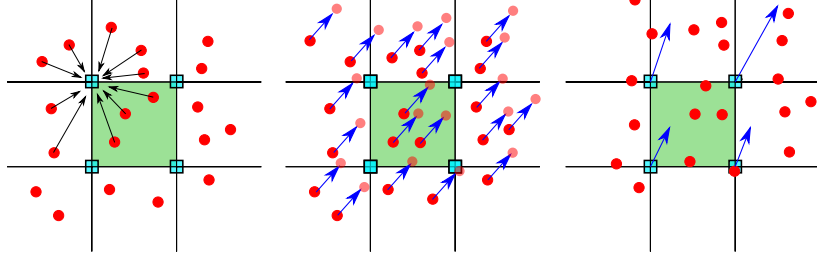
Figure 3: Description of the three steps in MPM standard algorithm.

However, as Andersen (2009)[31] pointed out, this algorithm has been shown to be numerically unstable due to that $\vec{f}_I^{int,k}$ can be infinite for an infinitesimal nodal mass $\mathbf{m}_I$. This issue may lead to numerical problems when nodal acceleration is obtained in the evaluation of the Eqs. (21) and (20). Hence, a corrected version of this algorithm was proposed by Zhang *et al.* (2016)[29]:

$$\vec{x}_p^{k+1} = \vec{x}_p^k + \sum_{I \in \mathcal{B}_p} \Delta t \, \frac{N_{Ip}^k \, \vec{p}_I^k}{\mathbf{m}_I}, \tag{22}$$

$$\vec{v}_p^{k+1} = \vec{v}_p^k + \sum_{I \in \mathcal{B}_p} \Delta t \, \frac{N_{Ip}^k \, \vec{f}_I^k}{\mathbf{m}_I}. \tag{23}$$

Delving into the improvement of the accuracy of the MPM explicit schemes, Tran & Solowski (2019)[20] presented a generalized-α scheme for MPM inspired in the explicit time integration algorithm proposed by Chung & Hulbert (1993)[27], but with the particularity that the acceleration is evaluated both in the beginning and the end of the time step.

$$\vec{v}_p^{k+1} = \vec{v}_p^k + \sum_{I \in \mathcal{B}_p} \Delta t \, N_{Ip}^k \, \left[(1 - \gamma) \, \vec{a}_I^k + \gamma \, \vec{a}_I^{k+1} \right], \tag{24}$$

$$\vec{x}_p^{k+1} = \vec{x}_p^k + \sum_{I \in \mathcal{B}_p} N_{Ip}^k \left[\Delta t \, \vec{v}_I^k + \Delta t^2 \left((\frac{1}{2} - \beta) \, \vec{a}_I^k + \beta \, \vec{a}_I^{k+1} \right) \right], \tag{25}$$

$$\vec{a}_p^{k+1} = \sum_{I \in \mathcal{B}_p} N_{Ip}^k \, \vec{a}_I^{k+1}. \tag{26}$$

140   This scheme has been proven to damp out the highest frequency noises [20]. However, it can present the same numerical instabilities as in (21),(20) when nodal masses become infinitesimal, and requires extra storage for nodal values of acceleration and previous steps.

11

In this section, an explicit predictor-corrector time integration scheme is proposed. It is based on the Newmark central differences explicit scheme, which is also referred to as a-form $\gamma = 0.5$ and $\beta = 0$. This method is devoted to solve a system of equations of the type

$$\sum_{J \in \mathcal{B}} \mathbf{M}_{IJ} \ddot{\mathbf{d}}_J + \mathbf{C}_{IJ} \dot{\mathbf{d}}_J + \mathbf{K}_{IJ} \mathbf{d}_J = \mathbf{F}_I.$$

The nodal MPM stage allows to apply this method within the MPM framework in a similar manner that the one proposed by Tran *et al.* [20]. By using the predictor definition, it is possible to calculate nodal velocities and update particles position employing nodal values of velocity and acceleration.

The predictor-corrector algorithm has been described in the classic literature [32], and its stability and computational advantages were widely validated by Liu [33]. The "classic" Newmark Predictor-Corrector (NPC) algorithm starts with a predicted value of the nodal velocities at the $(k+1)$th time step, denoted by $\vec{\tilde{v}}_I^{k+1}$, which is calculated as follows:

$$\vec{\tilde{v}}_I^{k+1} = \vec{v}_I^k + (1 - \gamma) \, \Delta t \, \vec{a}_I^k. \tag{27}$$

The *user-defined* parameter $\gamma \geq 0$ that appears in In (27), influences both the predictor accuracy and the stability of the algorithm. As pointed out Liu [33], the truncation error of the predictor formula is $O(\Delta t^3)$ when $\gamma = 0.5$, and is unconditionally stable if $0 < \gamma \leq 0.25$.

To accommodate this step to MPM framework, it is necessary to get the nodal values of the velocity and acceleration throughout a variational recovery process where particles quantities are transferred to the mesh nodes. This technique arises as a generalization of the super-convergent recovery procedures described by Zienkiewicz & Zhu [34] (*ZZ*) in the context of FEM. In MPM, Gauss quadratures are not employed. However, integrals are computed following the Riemann integral definition, where each component of the summation corresponds to a particle of the discretisation. Also Bardenhagen & Kober [3] proved that through this information-transference technique mass and momentum are conserved. So for a general particle variable Φ_p, employing the *ZZ* technique, it is possible to get its nodal homologous Φ_I as:

$$\Phi_I = \sum_{p \in \mathcal{C}} \frac{m_p N_{Ip} \Phi_p}{m_I}. \tag{28}$$

Therefore, to get an analogous expression for (27) in the context of MPM, the procedure described in the equation (28) is employed, obtainen the following

12

expression:

$$\vec{\tilde{v}}_I^{k+1} = \sum_{p \in \mathcal{C}} \underbrace{\frac{N_{Ip}^k m_p \vec{v}_p^k}{m_I}}_{\vec{v}_I^k} + (1 - \gamma) \, \Delta t \, \underbrace{\frac{N_{Ip}^k m_p \vec{a}_p^k}{m_I}}_{\vec{a}_I^k}. \tag{29}$$

Nonetheless this way of computing the predictor stage can introduce instabilities due to numerical cancellation likewise the original Sulky algorithm. Thankfully, this can be avoided easily by the equivalent formulation proposed as follows:

$$\vec{\tilde{v}}_I^{k+1} = \sum_{p \in \mathcal{C}} \frac{N_{Ip}^k m_p (\vec{v}_p^k + (1 - \gamma) \, \Delta t \, \vec{a}_p^k)}{m_I}. \tag{30}$$

This way of computing the nodal predictor is both numerically stable and minimize the computational effort. Once nodal velocities are obtained, the DBC are imposed over Γ_d. And in the following, the "classic" MPM algorithm continues to reach to the equilibrium equation (16). Next, the *corrector* stage is introduced. As nodal velocities were obtained earlier, this step is computed in the same way as in FEM,

$$\vec{v}_I^{k+1} = \vec{v}_I^{pred} + \gamma \, \Delta t \, \frac{\vec{f}_I^{k+1}}{\mathbf{m}_I^{k+1}}. \tag{31}$$

Finally updated particle accelerations, velocities and positions are updated as,

$$\vec{a}_p^{k+1} = \sum_{I \in \mathcal{B}_p} \frac{N_{Ip}^k \vec{f}_I^k}{\mathbf{m}_I^k} \tag{32}$$

$$\vec{v}_p^{k+1} = \vec{v}_p^n + \sum_{I \in \mathcal{B}_p} \Delta t \, \frac{N_{Ip}^k \, \vec{f}_I^k}{\mathbf{m}_I^k} \tag{33}$$

$$\vec{x}_p^{k+1} = \vec{x}_p^n + \sum_{I \in \mathcal{B}_p} \Delta t \, N_{Ip}^k \, \vec{v}_I^k + \frac{1}{2} \Delta t^2 \, \frac{N_{Ip}^k \, \vec{f}_I^k}{\mathbf{m}_I^k}. \tag{34}$$

Notice that particle displacements are computed using the corrected nodal velocities as well as the accelerations with the velocities of the predictor. However, particle velocities and accelerations are computed using the corrected velocities. Therefore here we share similarities with the *leapfrog scheme* where position is not updated at full time step, but the velocity is updated at half time steps. Notice also that, with this approach, the calculation of nodal momentum values are not required. Due to its simplicity, the proposed scheme can be implemented with minor modifications over the standard forward Euler. The full implementation is summarized in the algorithm .

Algorithm 1 Newmark Predictor-Corrector (NPC) scheme

1: **Update mass matrix**.

2: **Explicit Newmark Predictor**:

$$\vec{v}_I^{pred} = \sum_{p \, \in \, \mathcal{C}} \frac{N_{Ip}^k m_p(\vec{v}_p^k + (1 - \gamma) \, \Delta t \, \vec{a}_p^k)}{m_I}.$$

3: **Impose essential boundary conditions**:
At the fixed boundary, set $\vec{v}_I^{pred} = 0$.

4: **Deformation tensor increment calculation**.

$$\dot{\varepsilon}_p^{\,k+1} = \sum_{I \, \in \, \mathcal{B}_p} \left[\vec{v}_I^{pred} \otimes grad(N_{Ip}^{k+1}) \right]^s \quad \text{and} \quad \Delta \varepsilon_p^{k+1} = \Delta t \, \dot{\varepsilon}_p^{\,k+1}.$$

5: **Update the density field**:

$$\rho_p^{k+1} = \frac{\rho_p^k}{1 + trace \left[\Delta \varepsilon_p^{k+1} \right]}.$$

6: **Balance of forces calculation**:
Calculate the total grid nodal forces by evaluating the right hand side of (16) in the time step $k + 1$. In those nodes where $\frac{\partial \vec{v}_I^k}{\partial t}\big|_{\Gamma_d} = 0$, the acceleration is fixed to zero and nodal forces are stored as reactions.

7: **Explicit Newmark Corrector**:

$$\vec{v}_I^{k+1} = \vec{v}_I^{pred} + \gamma \, \Delta t \, \frac{\vec{f}_I^{k+1}}{\mathbf{m}_I^{k+1}}.$$

8: **Update particles lagrangian quantities**:

$$\vec{a}_p^{k+1} = \sum_{I \, \in \, \mathcal{B}_p} \frac{N_{Ip}^k \vec{f}_I^k}{\mathbf{m}_I^k},$$

$$\vec{v}_p^{k+1} = \vec{v}_p^n + \sum_{I \, \in \, \mathcal{B}_p} \Delta t \, \frac{N_{Ip}^k \, \vec{f}_I^k}{\mathbf{m}_I^k},$$

$$\vec{x}_p^{k+1} = \vec{x}_p^n + \sum_{I \, \in \, \mathcal{B}_p} \Delta t \, N_{Ip}^k \, \vec{v}_I^k + \frac{1}{2} \Delta t^2 \, \frac{N_{Ip}^k \, \vec{f}_I^k}{\mathbf{m}_I^k}.$$

9: **Reset nodal values**.

2.3. Local Max-Ent approximants

The popularity of the MPM has increased notoriously during the recent years due to its ability to deal with large strain problems without mesh distorsion issues inherent to mesh based methods like FEM, see Więckowski [35]. However, in the simulations made with the original MPM, numerical noises appear when particles cross the cell boundaries. Solving this issue is the main goal of the employment of the LME shape functions.

Local Maximum-Entropy (LME) approximation schemes were first introduced by Arroyo & Ortiz (2006)[10] and has been recently tested under MPM framework by Wobbes *et al.* (2020)[19]. The simulations presented in [19] of MPM within LME show considerably more accurate stress approximations than traditional MPM schemes. However, how the regularization parameter β affects to the accuracy and stability of the solution is not assessed deeply in that research. The tuning of this β parameter allows to make the comparison of the accuracy against analogous traditional MPM shape function.

The basic idea of the shape functions based on such an estimate is to interpret the shape function $N_I(\vec{x})$ as a probability. This allows us to introduce two important limits: the principle of maximum-entropy (*max-ent*) statistical inference stated by [36], and the Delaunay triangulation which ensures the minimal width of the shape function.

This approximation scheme represents an optimal compromise, in the sense of Pareto, between the *unbiased statistical inference* based on the nodal data which leads to the principle of *Maximum-Entropy* stated by Jaynes [36], and the definition of local shape functions of *least width* the least biased shape functions.

Taking the definition of entropy as a measure of how uncertainty a random variable is averaged on all its possible outcomes. And adopting the Shannon's entropy as the starting point:

$$H(p_1(\vec{x}), \ldots, p_n(\vec{x})) = -\sum_{I=1}^{N_n} p_I(\vec{x}) \log p_I \tag{35}$$

where $p_I(\vec{x})$ is the probability, equivalent to the mentioned shape function $N_I(\vec{x})$, satisfying both the zeroth and first-order consistency. The least-biased

approximation scheme is given by

$$\text{(LME) Maximize } H(N_I) \equiv -\sum_{I}^{N_n} N_I(\vec{x}) \log N_I$$

$$\text{subject to} \begin{cases} N_I \geq 0, \ I=1, \ ..., \ n \\[2ex] \sum_{I=1}^{N_n} N_I = 1 \\[2ex] \sum_{I=1}^{N_n} N_I \vec{x}_I = \vec{x} \end{cases}$$

On the other hand, the control of the shape function width and its decay with distance away from the corresponding nodes is a desirable property. To reach to this objective [10] propose the following linear program,

$$\text{(RAJ) For fixed } \vec{x} \text{ minimize } U(\vec{x}_p, N_I) \equiv \sum_{I} N_I |\vec{x}_p - \vec{x}_I|^2$$

$$\text{subject to} \begin{cases} N_I \geq 0, \ I=1, \ ..., \ n \\[2ex] \sum_{I=1}^{N_n} N_I = 1 \\[2ex] \sum_{I=1}^{N_n} N_I \vec{x}_I = \vec{x} \end{cases}$$

To reach to a compromise between two competing objectives, a Pareto set is defined by [10] as,

$$\text{(LME)}_\beta \text{ For fixed } \vec{x} \text{ minimize } f_\beta(\vec{x}, N_I) \equiv \beta U(\vec{x}, N_I) - H(N_I)$$

$$\text{subject to} \begin{cases} N_I \geq 0, \ I=1, \ ..., \ n \\[2ex] \sum_{I=1}^{N_n} N_I = 1 \\[2ex] \sum_{I=1}^{N_n} N_I \vec{x}_I = \vec{x} \end{cases}$$

The regularization or *thermalization* parameter between the two criterion, β, has Pareto optimal values in the range $\beta \in (0, \infty)$. The unique solution of the local *max-ent* problem LME_β is:

$$N_I^*(\vec{x}) = \frac{\exp\left[-\beta |\vec{x} - \vec{x}_I|^2 + \vec{\lambda}^* \cdot (\vec{x} - \vec{x}_I)\right]}{Z(\vec{x}, \vec{\lambda}^*)} \tag{36}$$

where

$$Z(\vec{x}, \vec{\lambda}) = \sum_{I=1}^{N_n} \exp\left[-\beta \left|\vec{x} - \vec{x}_I\right|^2 + \vec{\lambda} \cdot (\vec{x} - \vec{x}_I)\right] \tag{37}$$

being $\vec{\lambda}^*(\vec{x})$ the unique minimiser for the function $\log Z(\vec{x}, \vec{\lambda})$. The traditional way to obtain such a minimiser is using Eq. (38) to calculate small increments of $\partial\vec{\lambda}$ in a Newton-Raphson approach. $\mathbf{J}$ is defined as the Hessian matrix, obtained by:

$$\mathbf{J}(\vec{x}, \vec{\lambda}, \beta) \;\equiv\; \frac{\partial\vec{r}}{\partial\vec{\lambda}} \tag{38}$$

$$\vec{r}(\vec{x}, \vec{\lambda}, \beta) \;\equiv\; \frac{\partial \log Z(\vec{x}, \vec{\lambda})}{\partial\vec{\lambda}} = \sum_{I}^{N_n} p_I(\vec{x}, \vec{\lambda}, \beta)\,(\vec{x} - \vec{x}_I) \tag{39}$$

In order to obtain the first derivatives of the shape function, it is also necessary to compute ∇N_I^*

$$\nabla N_I^* = N_I^* \left(\nabla f_I^* - \sum_{J}^{N_n} N_J^* \nabla f_J^*\right) \tag{40}$$

where

$$f_I^*(\vec{x}, \vec{\lambda}, \beta) = -\beta \left|\vec{x} - \vec{x}_I\right|^2 + \vec{\lambda}\,(\vec{x} - \vec{x}_I) \tag{41}$$

Employing the chain rule, rearranging and considering β as a constant, Arroyo and Ortiz [10] obtained the following expression for the gradient of the shape function.

$$\nabla N_I^* \;=\; -N_I^* \left(\mathbf{J}^*\right)^{-1} (\vec{x} - \vec{x}_I) \tag{42}$$

The regularization parameter β of LME shape functions may be controlled by adjusting a dimensionless parameter, $\gamma = \beta h^2$ [10], where h is defined as a measure of the nodal spacing. Since N_I is defined in the entire domain, in practice, the function $\exp(-\beta\vec{r})$ truncated by a given tolerance, 10^{-6} in this research, would ensure a reasonable range of neighbours (see [10] for details). This tolerance defines the limit values of the influence radius and is used thereafter to find the neighbour nodes of a given integration point. An additional remark is that, analogous to alternative non-polynomial meshfree basis functions, the LME approximation scheme requires more than $d + 1$ nodes to determine the values of the shape functions as well as their derivatives at any point in the convex hull of the nodal set, where d is the dimension of the problem.

₂₀₅ This interpolation technique avoids important shortcomings when using GIMP or B-Spline MPM regarding the computational domain boundaries (see Steffen *et al.* (2008)[37]), which are related to the additional considerations in the application of the boundary conditions. Motivated by their increased extents, particles may share an influence radius that lies outside of ₂₁₀ the simulation domain. Some researchers have solved this problem with the so called "extra" or "ghost" nodes. These nodes require especial treatment, similar to those employed in the Smoothed Particle Hydrodynamics (SPH), for further details see Liu & Liu (2003)[38]. The approach here described does not requires the employment of this artifices. Due to the FEM-compatibility, ₂₁₅ the LME shape function is degenerated to linear finite element shape function if $d + 1$ neighbouring nodes are chosen as the support, where d is the number of dimensions in the problem. Ullah *et al.* [39] took advantage of the LME FEM-compatibility to couple the Element-Free Galerkin Method (EFGM) and FEM for linear elasticity and for problems with both material ₂₂₀ and geometrical non-linearities. Furthermore, with a conveniently adopted *regularization* parameter it is possible to get a GIMP-like shape function. Finally SPH-like behaviour can be obtained for lower values of γ since the support of the shape function is drastically increased, and therefore *smoother* solutions are obtained. See [15] for an application of this capability, where ₂₂₅ oscillations due to excess of pore water pressure in consolidation problems are smoothed out by using this technique. The employment of smoothing algorithms is also straightforward in the fluid-solid interaction problems [40]. A proof of this statements is observed in figure 4, where the LME adaptability is illustrated.

₂₃₀ In this research and in [10], β is a scalar as the influence area of the shape function is controlled by the Euclidean norm, therefore the search area is geometrically a circle in 2D, or a sphere in 3D. Building upon the idea of anisotropic shape functions, [41] introduced an enhanced version of the original LME scheme, which uses an anisotropic support to deal with tensile ₂₃₅ instability. This is another benefit of the proposed methodology, that, although is out of the scope of the present document, will be incorporated in future research. Unfortunately, local *max-ent* approximation technique only provides an efficient tool to transfer information from particles to nodes and vice versa to the MPM. Hence, the difficulties of imposing DBC in the ₂₄₀ MPM persists since they are a direct consequence of discretising the continuum with material points instead of nodes, where traditionally DBC are imposed. However, any available technique employed to overcome this situation in the standard MPM can be translated to the *max-ent* one thanks to the Kronecker-Delta property inherent to it [10]. See for instance the work ₂₄₅ of Cortis *et al.* (2018) [42] .

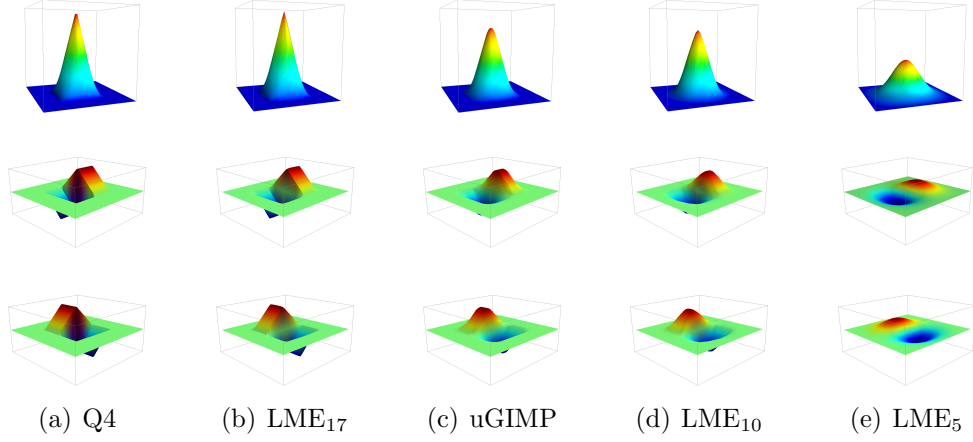(a) Q4　　　(b) LME$_{17}$　　　(c) uGIMP　　　(d) LME$_{10}$　　　(e) LME$_5$

Figure 4: Comparative of linear piecewise shape functions (Q4) and uGIMP shape functions *versus* LME approximation for a two-dimensional arrangement of nodes, and spatial derivatives for several values of $\gamma = \beta/h^2$.

3. Application to linear elasticity dynamic problems.

This section is devoted to test the ability of both predictor-corrector time integration scheme and the Local *Max-Ent* approximants to overcome spurious oscillations due to the grid crossing and high frequency loads under the context of MPM. Two different test have been adopted for this purpose: the benchmark proposed by Dyka & Ingel (1995)[43] and the test proposed in the PhD thesis of Andersen (2009)[31]. On the one hand, the accuracy of the Newmark Predictor-Corrector (NPC) scheme is compared to the standard Forward Euler (FE) in order to assess the performance of the time integration schemes. On the other hand, LME solutions are compared with those provided by Uniform GIMP (uGIMP) and Q4 shape functions. To avoid some mesh-dependent issues, in all calculations a regular background mesh was set. All simulations were performed with in-house software.

3.1. Dyka's bar [43]

This benchmark was proposed by Dyka [43] since allows to study easily the capability of the proposed time integration algorithm to avoid velocity field instabilities. It consists of a one-dimensional bar of a length of 0.1333 meters, sketched in the figure 5. The boundary conditions are: displacements are constrained ($\vec{v}|_{x=L} = 0$) in the right border, being free on all other boundaries. An initial velocity of $\vec{v}_o = -5 \ m/s$ is given to the left quarter of the bar. Finally, the elastic parameters chosen for this test are:

- Density : 7833 $kg/m3$
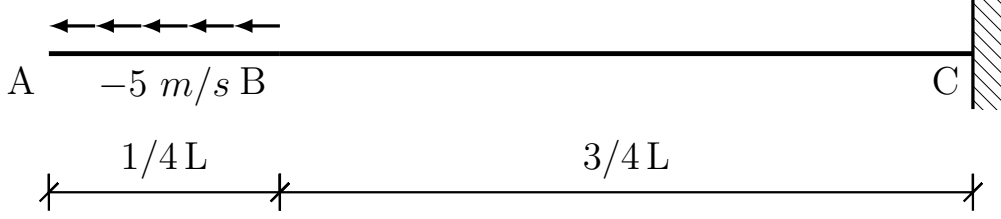
Figure 5: Geometrical description of the Dyka [43] bar.

- Poisson ratio : 0

- Elastic modulus : $200 \cdot 10^9 \; Pa$

In the proposed example, the simulation extends from time zero up to 0.00001 s. This time interval allows the elastic wave to travel a distance of 2.6 lengths of the bar. For the spatial discretisation, a set of seven nodal mesh sizes (0.1, 0.3325, 0.5, 1.0, 3.3325, 6.665, 10.0 millimeters) are considered. For each element a number of four particles was selected. In the initial layout, particles are located the exact quadrature points of a linear quadrilateral, with the exception of the uGIMP simulation, where gaps or overlap between voxels of each particle are not allowed. In those cases, each particle occupies the center of each cell quarter. For all simulations, time step is controlled by a Courant-Friedrichs-Levy condition of 0.1, were the adopted celerity is computed as:

$$Cel = \max\{\max_{p \in \Omega_p}\{\vec{v}_p\}, \max_{p \in \Omega_p}\{\sqrt{\frac{E_p}{\rho_p}}\}\}. \tag{43}$$

270   An important consideration regarding modellization concerns the background mesh. Notice that free border of the bar has a maximum horizontal displacement of 0.03 millimeters, therefore a computational domain with an extra gap of 0.03 millimeters is required in order to accommodate the unconstrained displacement of the particles in the left border of the bar. Naturally this prob-
275   lem arises when the mesh size is small enough that relative displacement of the particles is larger then the distance to the border, so grid crossing phenomena could appear even in those cases with infinitesimal displacements.

In this case, an analytical solution can be obtained through the characteristics method, described in the appendix Appendix A. To measure the convergence of the solutions for the different time integration and approximation schemes the root-mean-square (RMS) error in the velocity field is
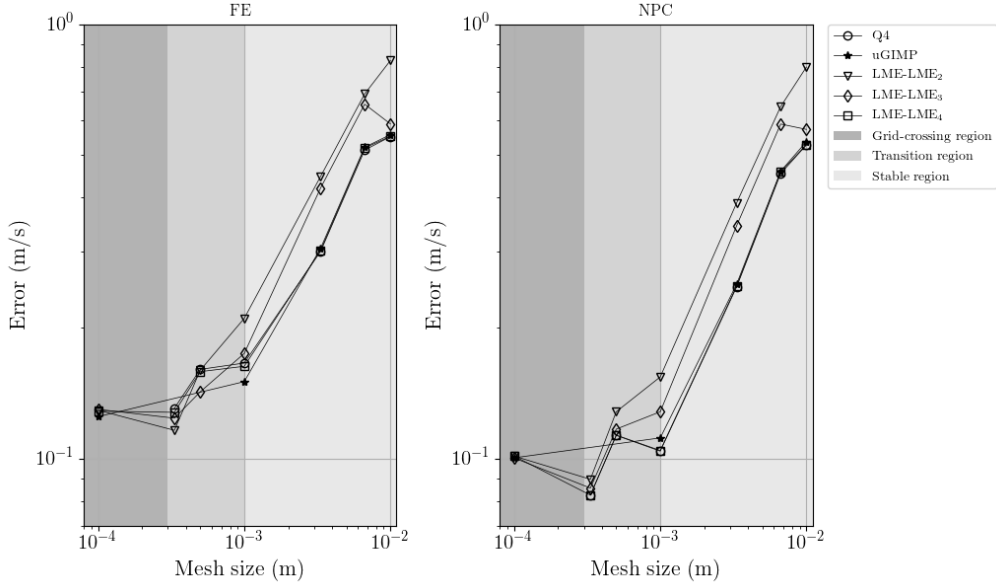
20

Figure 6: Velocity error evolution at the point A in the Dyka's bar , convergence plots for FE and NPC. The plot is subdivided with colours, the darker part of the diagram shows coincides when the relative movement of the particles is large enough to produce the grid crossing phenomena. The lightest part of the diagram coincides when the relative movement of the particles in negligible in comparison with the mesh size. And in the middle region a transition behaviour take place.

computed. RMS error is defined as

$$RMS = \sqrt{\frac{1}{N} \sum_{p}^{N} \left(\vec{v}_p - \hat{\vec{v}}_p \right)^2}, \qquad (44)$$

where $\vec{v}_p$ and $\hat{\vec{v}}_p$ are respectively the analytical and numerical solutions evaluated in the final time step in the position of each particle. In Fig. 6 the evolution of the RMS is obtained for both time integration schemes. The right figure, with the NPC results, shows lower values of the estimated error, denoting the higher performance of this methodology. About the spatial discretisation, the LME schemes show an error comparable to the obtained with the uGIMP, being even lower close to the grid-crossing region.

A first comparison between the obtained one in both time integration schemes is plotted in figure 7. It demonstrates the superior performance of the NPC *versus* the FE. In the NPC the spurious oscillations are quickly mitigated in the first time steps, and the error is not propagated in time,
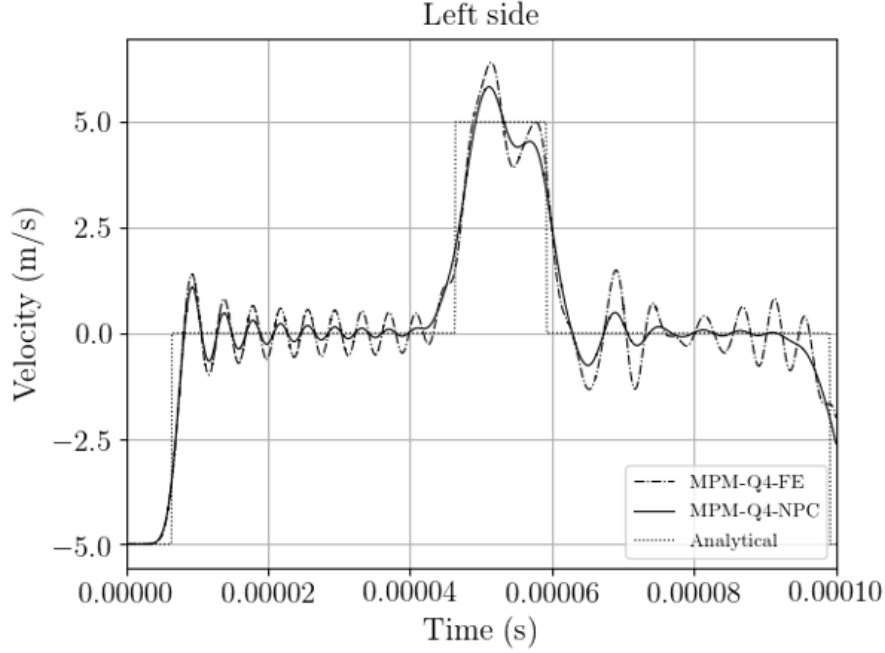
21

Figure 7: Comparison of NPC and FE performances: In the picture the velocity evolution at the point in the bar left side is plotted.

opposite to the results of the FE scheme, where the simulation becomes unstable after $6E^5$ seconds.

Figure (8) shows the sensitivity of the LME approximation scheme to variations in the parameter γ, which is the one that controls the value of the regularization parameter β together with of the mesh size. Notice how lower values of gamma exhibits a behaviour with a soft decay in some parts of the simulation due to the increase of nodes adopted to regularize the solutions. This capability could be useful in simulations where extremely noisy oscillations could damage the solutions like memory materials. On the other hand larger values of the parameter β make the solution to tend to the linear FEM solution as the athermal limit is reached [10]. Intermediate values of the regularization parameters give us a compromise between both scenarios described here. An additional observation, concerning to the solution sensibility depending on the regularization parameters, is the behaviour of the solution depending on the decreasing of mesh size. For larger mesh sizes, where the relative particle displacement is negligible in comparison with the cell size, the global behaviour is FEM-like; therefore, larger values of γ may offer better results. On the other hand, when mesh size is small enough to produce grid-crossing meshfree behaviour is required to ensure the conver-

22

gence of the solution and tiny values of γ may lead to better performances. Convergence plot in figure (6) shows how the slope, for the larger values of γ, decreases monotonically with the value of the mesh size, in contrast with larger values of γ, where the performance is punished with significant movement of the particles as far as the mesh size is reduced. The performance of the uGIMP [3] shape function *versus* the LME approximation scheme with a dimensionless regularization parameter γ of 4.0 is compared in Figure 9. Although remarkable differences are not observed, more robust behaviour is exhibited by the LME approximants than the uGIMP shape functions. Regarding this, notice the absence of uGIMP values for a mesh size of 0.3325 and 0.5 millimeters. The reason is due to an unstable increasing of the error suffered during uGIMP simulations of these mesh sizes which yield unacceptable results. A feasible explanation for this phenomena could be the presence of numerical cancellation which could produce gaps between voxels. Further research should be done in this direction for getting a better comprehension of this phenomenon. Conversely, this shortcoming is not suffered by LME, independently of regular or with irregular nodal layout.

Finally, the OTM [44] solution is compared against the one obtained with MPM, both with same time integration scheme and spatial discretisation, and results are shown in figure 10. In this case, the performance of MPM presents better robustness and stability than the OTM. During the first half of the simulation both method seem to perform in a similar way, but during the second half of the simulation after the elastic wave has travel from the free border to the fixed one and back, in OTM the solution becomes more noisy than the one performed by MPM.
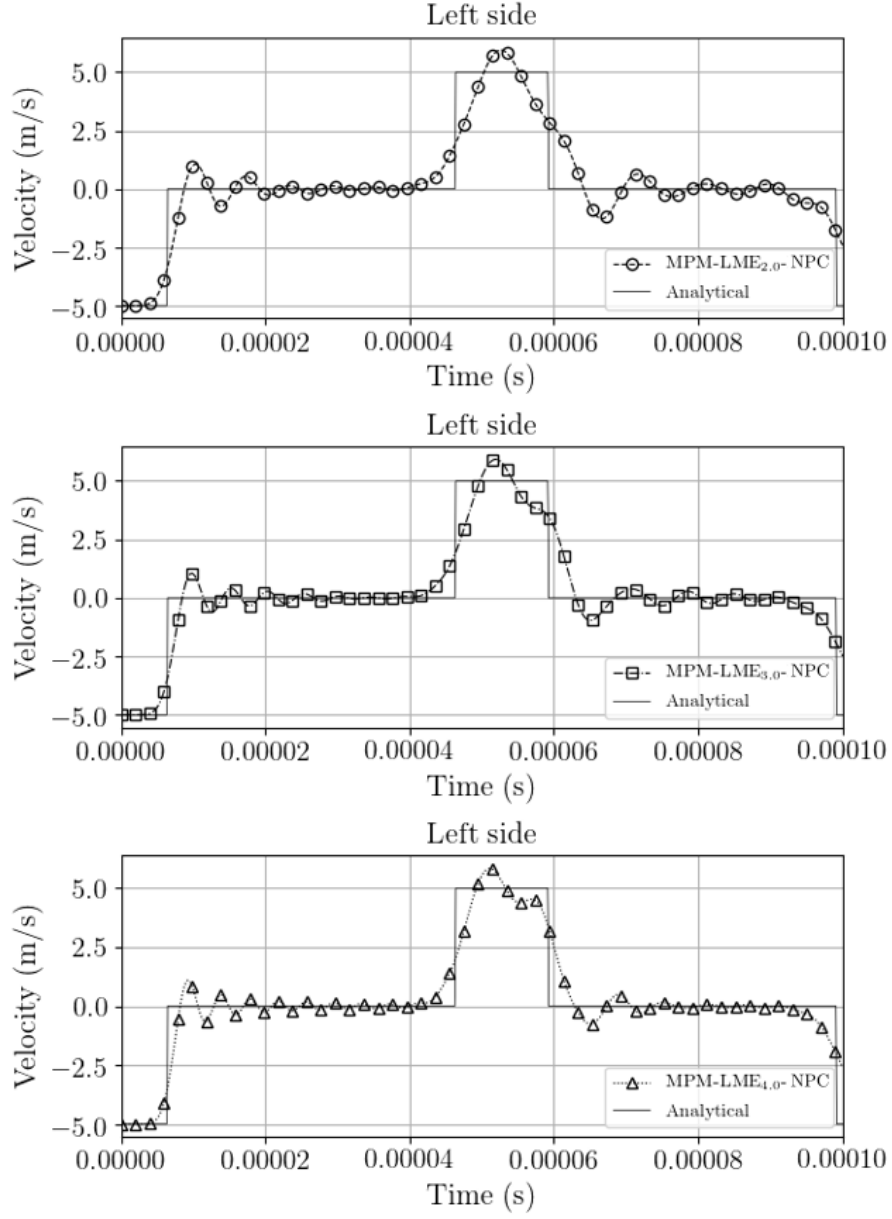
23

Figure 8: Sensitivity of LME approximants performance to changes in the dimensionless regularization parameter $\gamma = \beta/h^2$. To illustrate it, the velocity evolution at the point in the bar left side is plotted.
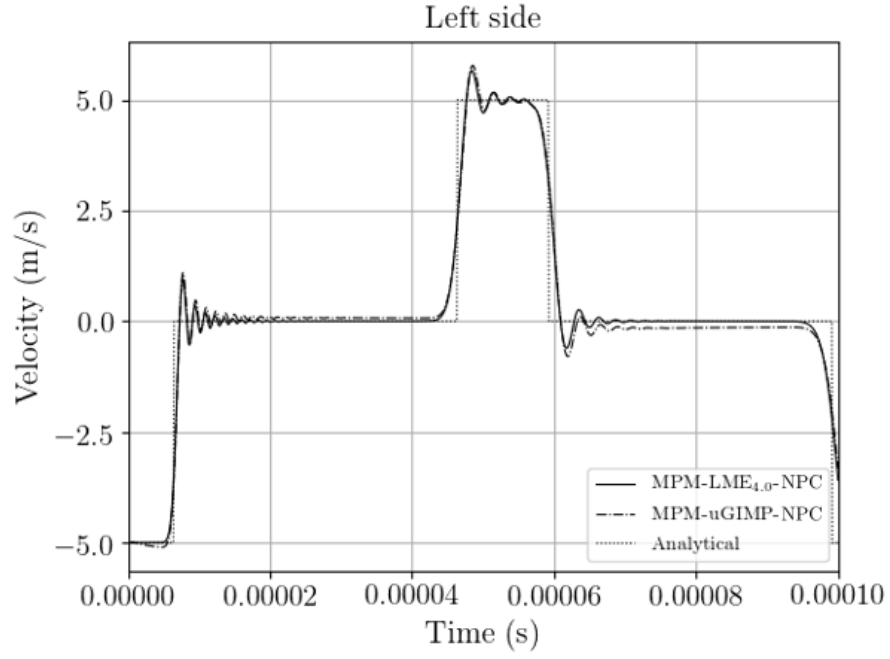
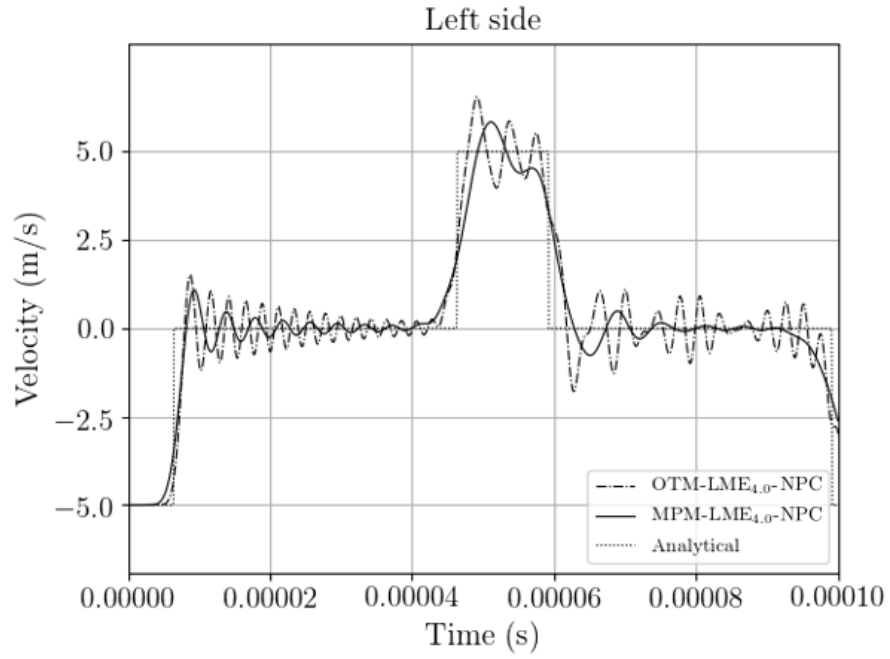Figure 9: Velocity evolution at the point in the bar left side.

Figure 10: Velocity evolution at the point in the bar left side.
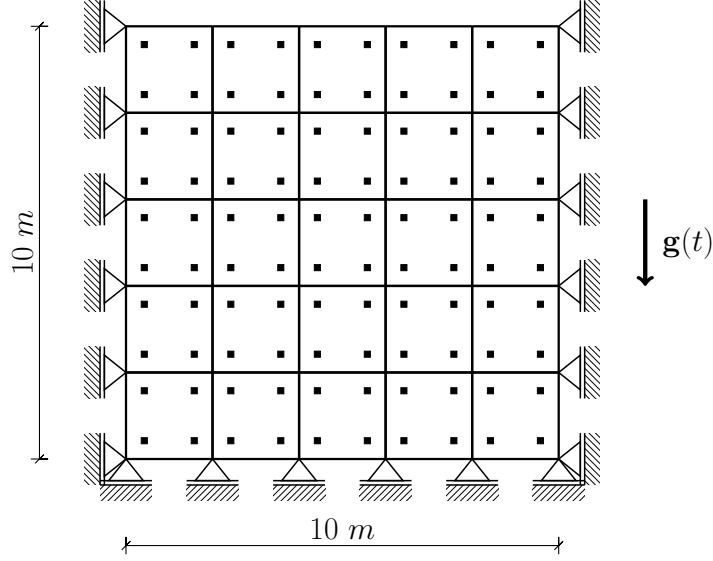
25

Figure 11: Geometrical description of a soil block
.

3.2. Rigid block

The following test was proposed to validate the ability of the proposed interpolation technique to deal with grid crossing instabilities. It consists of the simulation of a square block of soil incrementally loaded by a body force. Details of the problem are sketched in figure 11 This test was previously proposed by Andersen (2009)[31]. The elastic parameters considered for this test are:

- Initial density : $6 \cdot 10^3 \ kg/m^3$

- Poisson ratio : 0

- Elastic modulus : $5 \ MPa$

The gravity force is applied as an external force according to the equations (??) and (??). Using a total time period of T (20 seconds) to apply the gravity, it is increased from 0 to $9.81 m/s$ with a sinusoidal function until T/2 and then maintained constant until T in order to reach the equilibrium state:

$$\mathbf{g}(t) = \begin{cases} 0.5\mathbf{g}(\sin(\frac{2t\pi}{T} - \frac{\pi}{2}) + 1) & \text{if } t \leq T/2 \\ \mathbf{g} & \text{if } t > T/2 \end{cases} \tag{45}$$

In order to get a stable solution, time step was conducted by a Courant number of 0.1. On the other hand, the explicit predictor-corrector scheme is here
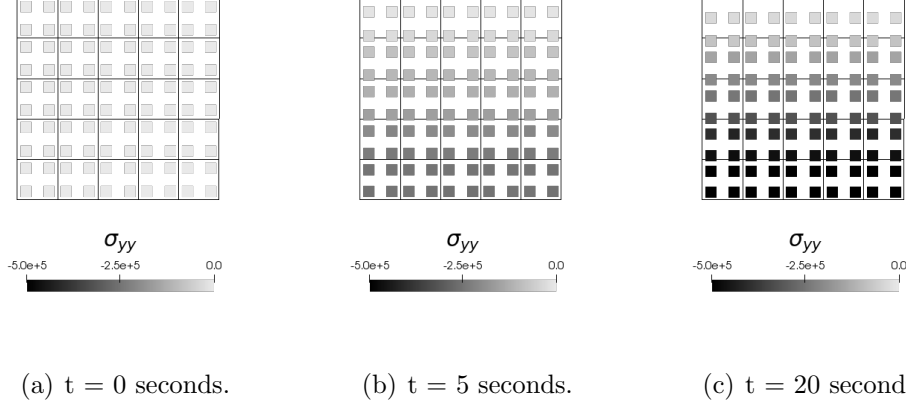
| (a) t = 0 seconds. | (b) t = 5 seconds. | (c) t = 20 seconds |

Figure 12: Vertical normal stress and position of material points during the loading process for a soft soil ($E = 5\ MPa$, $\rho_0 = 6 \cdot 10^3\ kg/m^3$). Numerical parameters considered for the simulation are : Local *max-ent* shape function $\gamma = 3$ and explicit PC scheme with CFL 0.1.

employed looking forward to getting better results. For the initial spatial discretisation four particles per cell ($\Delta x = 2\ m$) were adopted. The initial layout of particles inside of the cell changes according to the approximation technique adopted. For the bi-linear shape functions and the LME approximants, the initial position corresponds to the location of the gauss-points in a standard quadratic finite element. For the uGIMP shape function the initial position of each particle is located in the center of each voxel, due to the fact that in the initial situation, the voxel domain should not overlap each others.

Figure 12 shows the evolution of the vertical stress during the loading process. The result is physically realistic as the stress increases linearly from the top to the bottom of the specimen, and the value of the vertical stress in a material point located in the bottom of the specimen oscillates around $5.2MPa$, which is the analytic value given by $\sigma_{yy} = \rho g h_y$.

Figure 13 shows the vertical displacement evolution of a point in the free surface of the block. This figure shows how simulations performed with a bi-linear interpolation technique (Q4) turns out to be unstable during cell-crossing and consequently fail. The uGIMP simulation is more stable than the one performed by the Q4, although is still unstable and could trigger severe oscillations in simulation with non-linear materials. The LME simulation was performed using two kinds of shape functions, one with a low value of the dimensionless parameter, $\gamma = 0.8$, and other with a larger value of it, $\gamma = 3.0$. Notice that the results are both stable, but the larger values of γ give us a very stable solution. This is due to the fact that with larger
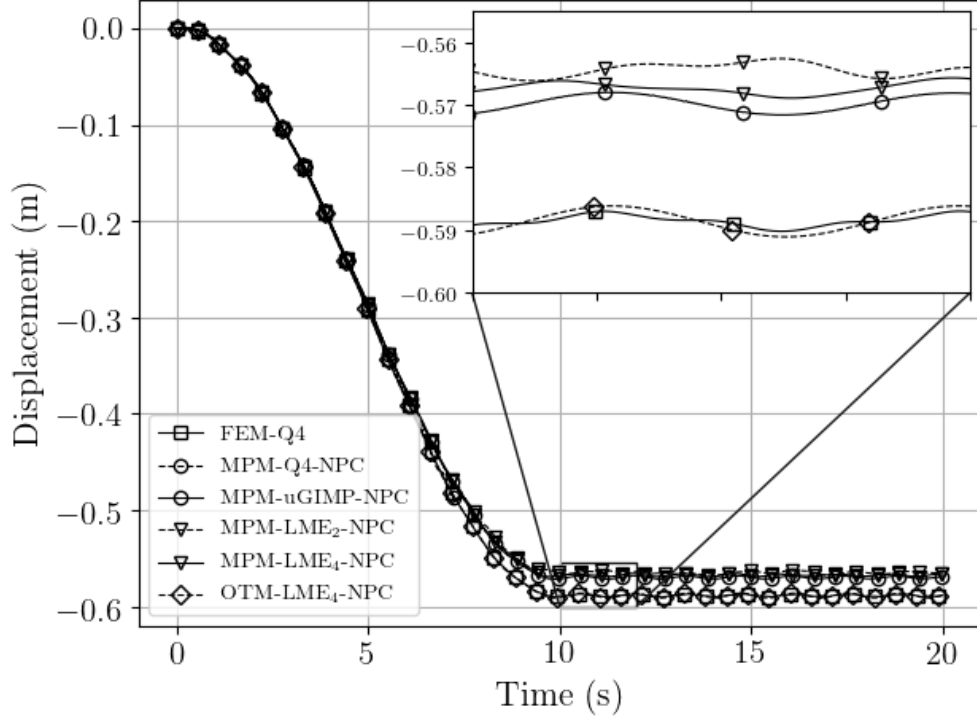
27

Figure 13: Comparative of the vertical displacement evolution in a point located in the free surface employing different interpolation schemes and numerical techniques.

value of γ, the shape functions behaves in a similar way to the FEM, which performs very accurate in those cases with a reasonable mesh distorsion, and with a lower value it behaves in a similar way to the uGIMP. This behaviour was noticed previously by [10], were authors highlighted how, by adjusting the spatial variation of $\beta(\vec{x})$, it is possible to select regions of the domain of analysis which are treated by finite elements and regions that are treated in the style of meshfree methods, with seamless transitions between those regions.

4. Conclusions

We have proposed in this paper an enhanced methodology which improves Material Point Method (MPM) behaviour in fast dynamics problems. Different time and space discretisation techniques have been presented and their performance being compared agains other approaches in two benchmark problems. First, a novel time integration scheme for MPM has been

28

carried out. The NPC has been shown to be a highly efficient alternative for demanding fast dynamics problems. In the literature, several approaches of the NPC are proposed in order to compete on accuracy with expensive implicit time integration algorithms. The main achievement of the proposed time discretisation has been observed within the Dyka's bar 3.1, obtaining lower values of the error than the ones obtained with the Forward Euler (FE) scheme. Also, the procedure employed to design the NPC algorithm opens the door to revisit a huge variety of time integration schemes developed originally for FEM, which can be implemented within a MPM framework with the suitable modifications. In addition to the implementation of enhanced time integration schemes, further research can be done in the analysis of the good performance of the algorithm within non-linear solutions, such as the coupling between different phases or the non-linear constitutive behaviour of the materials: the employment of this scheme to strengthen the localization capabilities of MPM for viscoplastic materials is on the scope of this research line. The comparison with traditional time schemes in the non-linear field will improve the formal understanding of the proposed methodology.

On the other hand, the spatial discretisation of the MPM is enhanced thanks to the powerful skills of the Local Maximum-Entropy (LME) approximation scheme, which has been validated as a robust and versatile tool in the MPM framework. It also comes up as a promising alternative to other approximation techniques, developed within the MPM framework, in order to overcome grid crossing limitations and to avoid the constriction of the uGIMP of a regular mesh or a high density of particles per cell. Several research lines of the LME scheme dive into the improvement of the methodology, focusing in the optimization of the calculation of the shape function and the possibility of adapting the parameter $\beta(\vec{x})$ through the finite strain tensor in order to align the shape functions in the principal strain direction to select the most suitable set of nodes adapted to the strain as well as the possibility of adapting the value of β to solve the equations FEM-like of meshfree-like depending of how behaves the region. Together with the implementation of non-linear behaviours, previously mentioned, challenging scenarios could be reproduced, being the main purpose of the research line the simultaneous simulation of both initialization and propagation stages of fast landslides.

Conflict of interest

The authors declare that they have no conflict of interest.

29

Appendix A. The analytical solution of the 1D Dyka benchmark

For the derivation of this analytical solution, a 1D elastic bar is consider. Henceforth for convenience the governing equations will be written in terms of stress and velocity. The balance of linear momentum,

$$\rho \, \frac{\partial v}{\partial t} = \frac{\partial \sigma}{\partial x}, \tag{A.1}$$

Secondly the constitutive equation is the well known linear elastic one,

$$\frac{\partial \sigma}{\partial t} = E \frac{\partial \varepsilon}{\partial t}, \tag{A.2}$$

where E is the elastic modulus. And finally the compatibility equation,

$$\frac{\partial \varepsilon}{\partial t} = \frac{\partial v}{\partial x}. \tag{A.3}$$

Next for simplicity, we will introduce (A.3) in (A.2), it yield to,

$$\frac{\partial v}{\partial t} = \frac{1}{\rho} \, \frac{\partial \sigma}{\partial x}, \tag{A.4}$$

$$\frac{\partial \sigma}{\partial t} = E \, \frac{\partial v}{\partial x}. \tag{A.5}$$

Introducing (A.5) in (A.4) and expressing the remaining equation in terms of the displacement, results the wave equation for linear elastic materials,

$$\frac{\partial^2 u}{\partial t^2} = \frac{E}{\rho} \, \frac{\partial^2 u}{\partial x^2} = c^2 \, \frac{\partial^2 u}{\partial x^2} \tag{A.6}$$

where $c = \sqrt{\frac{E}{\rho}}$ is the material celerity. Alternative, rearranging both equations (A.4) and (A.5) it is possible to join them in a single system of equations as,

$$\frac{\partial}{\partial t} \begin{bmatrix} \sigma \\ v \end{bmatrix} + \begin{bmatrix} 0 & -E \\ -1/\rho & 0 \end{bmatrix} \begin{bmatrix} \frac{\partial \sigma}{\partial x} \\ \frac{\partial v}{\partial x} \end{bmatrix} = \mathbf{0}. \tag{A.7}$$

Or in a more compact format,

$$\frac{\partial \phi}{\partial t} + \mathbf{A}\frac{\partial \phi}{\partial x} = \mathbf{0}. \tag{A.8}$$

In (A.8) stress and velocity are joined in to a single structure ϕ and $\mathbf{A}$ in coupling matrix between both equations,

$$\phi = \begin{bmatrix} \sigma \\ v \end{bmatrix}, \quad \mathbf{A} = \begin{bmatrix} 0 & -E \\ -1/\rho & 0 \end{bmatrix}.$$

Despite of this manipulation, the nature of is still hyperbolic. A proof of this can be easily obtained computing the zeros of the hypersurface defined by (A.6). And later the eigenvalues of $\mathbf{A}$ in (A.8). In both cases, eigenvalues are real and distinct ($\lambda = \pm\sqrt{\frac{E}{\rho}}$), therefore the system is called strictly hyperbolic. Assuming that $\mathbf{A}$ has n different eigenvalues $\{\lambda_1, \ldots, \lambda_i, \ldots \lambda_n\}$ and n eigenvectors $\{\vec{x}^1, \ldots, \vec{x}^i, \ldots \vec{x}^n\}$ satisfying that $\mathbf{A}\vec{x} = \lambda\vec{x}$. Now we introduce the matrix $\mathbf{P}$ whose columns are the n eigenvalues $\mathbf{x}$

$$\mathbf{P} = \{\vec{x}^1, \vec{x}^2, \vec{x}^3, \ldots \vec{x}^n\}. \tag{A.9}$$

Diagonalizing $\mathbf{A}$ using $\mathbf{P}$ yields,

$$\Lambda = \mathbf{P}^{-1}\mathbf{A}\,\mathbf{P}, \tag{A.10}$$

where $\Lambda_{ii} = \lambda_i$. Now, lets define a vector $\Re$ as

$$\phi = \mathbf{P}\,\Re. \tag{A.11}$$

Expanding the above expression with the chain rule and passing the matrix $\mathbf{P}$ to left hand side of the equality we get,

$$d\vec{\Re} = \frac{\partial \Re}{\partial t}dt + \frac{\partial \Re}{\partial x}dx = \mathbf{P}^{-1}\left(\frac{\partial \phi}{\partial t}dt + \frac{\partial \phi}{\partial x}dx\right) \tag{A.12}$$

and setting the terms we get,

$$\frac{\partial \Re}{\partial t} = \mathbf{P}^{-1}\frac{\partial \phi}{\partial t}, \quad \frac{\partial \Re}{\partial x} = \mathbf{P}^{-1}\frac{\partial \phi}{\partial x} \tag{A.13}$$

Next, if we multiply (A.8) by $\mathbf{P}^{-1}$ we get:

$$\mathbf{P}^{-1}\frac{\partial \phi}{\partial t} + \left(\mathbf{P}^{-1}\mathbf{A}\mathbf{P}\right)\mathbf{P}^{-1}\frac{\partial \phi}{\partial x} = \mathbf{0} \tag{A.14}$$

31

finally introducing the expressions (A.13) we reach to

$$\frac{\partial \Re}{\partial t} + \Lambda \frac{\partial \Re}{\partial x} = \mathbf{0} \tag{A.15}$$

which consists of n uncoupled equations as Λ is diagonal matrix as we can see in (A.10). Each of this equations are 1D scalar convective transport equations, with solutions of the form:

$$\Re^{(i)} = F^{(i)}\left(x - \lambda^{(i)}t\right) \tag{A.16}$$

This uncoupled system, has a set of n characteristics. These magnitudes $\Re_i$ which propagate along characteristics are known as *Riemann invariants* of the problem. For the closure of the problem it is required "n" initial conditions of the form $\Re_i(x, t = 0) = h_i(x)$, and "n" boundary conditions. Particularizing the previous equations for the 1D elastic bar described in [43], $\mathbf{P}$ can computed as,

$$\mathbf{P} = \left[\begin{array}{cc} -\sqrt{E\rho} & \sqrt{E\rho} \\ 1 & 1 \end{array} \right]$$

With the value of the inverse matrix $\mathbf{P}^{-1}$ in the Riemann definition (A.11), a set of equations arise,

$$\Re^{I} = \frac{1}{2\sqrt{\rho E}}\left(-\sigma + v \sqrt{\rho E}\right) \tag{A.17}$$

$$\Re^{II} = \frac{1}{2\sqrt{\rho E}}\left(\sigma + v \sqrt{\rho E}\right) \tag{A.18}$$

From (A.17) and (A.18) the values of the stress and the velocity can be computed in the following way,

$$v = \Re^{I} + \Re^{II} \quad , \quad \sigma = \sqrt{E\rho}\left(\Re^{II} - \Re^{I}\right) \tag{A.19}$$

The boundary conditions are in both cases of radiation as there is not wave in-going from the exterior. So for the right side the conditions are,

$$\Re^{II} = 0 \quad and \quad v_{x=L} = 0 \quad \Rightarrow \quad \sigma_{x=L} = -2\sqrt{\rho E}\ \Re^{I}$$

And in the left side,

$$\Re^{I} = 0 \quad and \quad \sigma_{x=0} = 0 \quad \Rightarrow \quad v_{x=0} = 2\Re^{II}$$

By imposing this boundary conditions, the problem is fully defined as in [43].

References

[1] D. L. Sulsky, H. Schreyer, Z. Chen, A particle method for history-dependent materials, Computer Methods in Applied Mechanics and Engineering 118 (1) (1994) 179–196. `doi:10.1016/0045-7825(94)90112-0`.

[2] J. U. Brackbill, H. M. Ruppel, FLIP: A method for adaptively zoned, particle-in-cell calculations of fluid flows in two dimensions, Journal of Computational Physics`doi:10.1016/0021-9991(86)90211-1`.

[3] S. G. S. G. Bardenhagen, E. M. Kober, The generalized interpolation material point method, CMES - Computer Modeling in Engineering and Sciences 5 (6) (2004) 477–495.

[4] M. Steffen, R. M. Kirby, M. Berzins, Analysis and reduction of quadrature errors in the material point method (MPM), International Journal for Numerical Methods in Engineering 76 (6) (2008) 922–948. `doi:10.1002/nme.2360`.
URL `http://doi.wiley.com/10.1002/nme.2360`

[5] D. Z. Zhang, X. Ma, P. T. Giguere, Material point method enhanced by modified gradient of shape function, Journal of Computational Physics 230 (16) (2011) 6379–6398. `doi:10.1016/J.JCP.2011.04.032`.
URL `https://www.sciencedirect.com/science/article/pii/S0021999111002804`

[6] T. R. Dhakal, D. Z. Zhang, Material point methods applied to one-dimensional shock waves and dual domain material point method with sub-points, Journal of Computational Physics 325 (2016) 301 – 313. `doi:https://doi.org/10.1016/j.jcp.2016.08.033`.
URL `http://www.sciencedirect.com/science/article/pii/S0021999116303904`

[7] A. Sadeghirad, R. M. Brannon, J. Burghardt, A convected particle domain interpolation technique to extend applicability of the material point method for problems involving massive deformations, International Journal for Numerical Methods in Engineering 86 (12) (2011) 1435–1456. `arXiv:https://onlinelibrary.wiley.com/doi/pdf/10.1002/nme.3110`, `doi:10.1002/nme.3110`.
URL `https://onlinelibrary.wiley.com/doi/abs/10.1002/nme.3110`

[8] R. Tielen, E. Wobbes, M. Möller, L. Beuth, A high order material point method, Procedia Engineering 175 (2017) 265 – 272, proceedings of the 1st International Conference on the Material Point Method (MPM 2017). `doi:https://doi.org/10.1016/j.proeng.2017.01.022`. URL `http://www.sciencedirect.com/science/article/pii/S187770581730022X`

[9] E. Wobbes, M. Moller, V. Galavi, C. Vuik, M. Möller, V. Galavi, C. Vuik, M. Moller, V. Galavi, C. Vuik, Conservative Taylor Least Squares reconstruction with application to material point methods: Conservative Taylor Least Squares reconstruction, International Journal for Numerical Methods in Engineering 117 (3) (2018) 271–290. `doi:10.1002/nme.5956`.

[10] M. Arroyo, M. Ortiz, Local maximum-entropy approximation schemes: A seamless bridge between finite elements and meshfree methods, International Journal for Numerical Methods in Engineering`doi:10.1002/nme.1534`.

[11] D. Millán, N. Sukumar, M. Arroyo, Cell-based maximum-entropy approximants, Comput. Meth. Appl. Mech. Engrg. 284 (2015) 712–731.

[12] B. Li, A. Kidane, G. Ravichandran, M. Ortiz, Verification and validation of the Optimal Transportation Meshfree (OTM) simulation of terminal ballistics, International Journal of Impact Engineering`doi:10.1016/j.ijimpeng.2011.11.003`.

[13] P. Navas, L. Sanavia, S. López-Querol, R. C. Yu, Explicit meshfree solution for large deformation dynamic problems in saturated porous media., Acta geotechnica 13 (2018) 227–242. `doi:10.1007/s11440-017-0612-7`.

[14] P. Navas, S. López-Querol, R. C. Yu, M. Pastor, Optimal transportation meshfree method in geotechnical engineering problems under large deformation regime, International Journal for Numerical Methods in Engineering`doi:10.1002/nme.5841`.

[15] P. Navas, S. López-Querol, R. C. Yu, B. Li, B-bar based algorithm applied to meshfree numerical schemes to solve unconfined seepage problems through porous media, Int. J. Numer. Anal. Methods Geomech. 40 (6) (2016) 962–984. `doi:10.1002/nag.2472`.

[16] P. Navas, R. C. Yu, S. López-Querol, B. Li, Dynamic consolidation problems in saturated soils solved through u-w formulation in a LME

34

meshfree framework, Comput. Geotech. 79 (2016) 55–72. `doi:10.1016/` `j.compgeo.2016.05.021`.

[17] P. Navas, L. Sanavia, S. López-Querol, R. C. Yu, u-w formulation for dynamic problems in large deformation regime solved through an implicit meshfree scheme., Comput. Mech. 62 (2018) 745–760. `doi:` `10.1007/s00466-017-1524-y`.

[18] C.Weißenfels, P.Wriggers, Stabilization algorithm for the optimal transportation meshfree approximation scheme, Comput. Meth. Appl. Mech. Engrg. 329 (2018) 421–443.

[19] E. Wobbes, R. Tielen, M. Möller, C. Vuik, Comparison and unification of material-point and optimal transportation meshfree methods, Computational Particle Mechanics`doi:10.1007/s40571-020-00316-7`.

[20] Q. A. Tran, W. Sołowski, Temporal and null-space filter for the material point method, International Journal for Numerical Methods in Engineering`doi:10.1002/nme.6138`.

[21] J. Guilkey, J. Weiss, Implicit time integration for the material point method: Quantitative and algorithmic comparisons with the finite element method, International Journal for Numerical Methods in Engineering 57 (2003) 1323 – 1338. `doi:10.1002/nme.729`.

[22] B. Wang, P. Vardon, M. Hicks, Z. Chen, Development of an implicit material point method for geotechnical applications, Computers and Geotechnics 71 (2016) 159–167. `doi:10.1016/j.compgeo.2015.08.` `008`.

[23] T. J. Charlton, W. M. Coombs, C. E. Augarde, iGIMP: An implicit generalised interpolation material point method for large deformations, Computers & Structures 190 (2017) 108–125. `doi:10.1016/` `j.compstruc.2017.05.004`.

[24] S. Kularathna, K. Soga, Implicit formulation of material point method for analysis of incompressible materials, Computer Methods in Applied Mechanics and Engineering 313 (2017) 673 – 686. `doi:https://doi.org/10.1016/j.cma.2016.10.013`.
    URL `http://www.sciencedirect.com/science/article/pii/` `S0045782516313081`

35

[25] M. Lu, J. Zhang, H. Zhang, Y. Zheng, Z. Chen, Time-discontinuous material point method for transient problems, Computer Methods in Applied Mechanics and Engineering 328 (2018) 663 – 685. doi:https://doi.org/10.1016/j.cma.2017.09.022.
URL http://www.sciencedirect.com/science/article/pii/S0045782517301779

[26] E. L. Wilson, I. Farhoomand, K. J. Bathe, Nonlinear dynamic analysis of complex structures, Earthquake Engineering & Structural Dynamics 1 (3) (1972) 241–252. doi:10.1002/eqe.4290010305.
URL http://doi.wiley.com/10.1002/eqe.4290010305

[27] J. Chung, G. M. Hulbert, A Time Integration Algorithm for Structural Dynamics With Improved Numerical Dissipation: The Generalized-alpha Method, J. Appl. Mech. 60 (2) (1993) 371. doi:10.1115/1.2900803.

[28] B. Riemann, Über die darstellbarkeit einer function durch eine trigonometrische reihe, Abhandlungen der Königlichen Gesellschaft der Wissenschaften zu Göttingen 13 (1854) 87 – 138. doi:https://doi.org/10.1016/j.cma.2017.09.022.

[29] X. Zhang, Z. Chen, Y. Liu, The Material Point Method: A Continuum-Based Particle Method for Extreme Loading Cases, Elsevier, 2016. doi:10.1016/b978-0-12-407716-4.00003-x.

[30] S. G. S. Bardenhagen, Energy Conservation Error in the Material Point Method for Solid Mechanics, Journal of Computational Physics 180 (1) (2002) 383–403. doi:10.1006/JCPH.2002.7103.

[31] S. M. Andersen, Material-Point Analysis of Large-Strain Problems: modelling of landslides, Ph.D. thesis, Department of Civil Engineering, Aalborg University (2009).

[32] T. J. R. Hughes, The finite element method : linear static and dynamic finite element analysis, Dover Publications, 2000.

[33] X. Liu, On the stability of a newmark's scheme-based predictor-corrector algorithm, Computers & Structures 53 (1994) 27–33. doi:10.1016/0045-7949(94)90126-0.

[34] O. C. Zienkiewicz, J. Z. Zhu, The superconvergent patch recovery and a posteriori error estimates. part 1: The recovery technique, International

Journal for Numerical Methods in Engineering 33 (7) (1992) 1331–1364. `doi:10.1002/nme.1620330702`.

[35] Z. Więckowski, The material point method in large strain engineering problems, Computer Methods in Applied Mechanics and Engineering 193 (39-41 SPEC. ISS.) (2004) 4417–4438. `doi:10.1016/j.cma.2004.01.035`.

[36] E. Jaynes, Information Theory and Statistical Mechanics, The Physical Review 106 (4) (1957) 620–630.

[37] M. Steffen, P. C. Wallstedt, J. Guilkey, R. M. Kirby, M. Berzins, Examination and analysis of implementation choices within the Material Point Method (MPM), CMES - Computer Modeling in Engineering and Sciences 31 (2) (2008) 107–127.

[38] G. R. G.-R. Liu, M. B. Liu, Smoothed particle hydrodynamics : a meshfree particle method, World Scientific, 2003.
URL `https://books.google.es/books/about/Smoothed{_}Particle{_}Hydrodynamics.html?id={_}cwFMmEQvZQC{&}redir{_}esc=y`

[39] Z. Ullah, W. Coombs, C. Augarde, An adaptive finite element/meshless coupled method based on local maximum entropy shape functions for linear and nonlinear problems, Computer Methods in Applied Mechanics and Engineering 267 (2013) 111 – 132. `doi:https://doi.org/10.1016/j.cma.2013.07.018`.
URL `http://www.sciencedirect.com/science/article/pii/S0045782513001941`

[40] W.-C. Yang, P. Arduino, G. R. Miller, P. Mackenzie-Helnwein, Smoothing algorithm for stabilization of the material point method for fluid–solid interaction problems, Computer Methods in Applied Mechanics and Engineering 342 (2018) 177 – 199. `doi:https://doi.org/10.1016/j.cma.2018.04.041`.
URL `http://www.sciencedirect.com/science/article/pii/S0045782518302263`

[41] S. Kumar, K. Danas, D. M. Kochmann, Enhanced local maximum-entropy approximation for stable meshfree simulations, Computer Methods in Applied Mechanics and Engineering`doi:10.1016/j.cma.2018.10.030`.

[42] M. Cortis, W. Coombs, C. Augarde, M. Brown, A. Brennan, S. Robinson, Imposition of essential boundary conditions in the material point method, International Journal for Numerical Methods in Engineering 113 (1) (2018) 130–152. `doi:10.1002/nme.5606`.
URL `http://doi.wiley.com/10.1002/nme.5606`

[43] C. Dyka, R. Ingel, An approach for tension instability in smoothed particle hydrodynamics (SPH), Computers & Structures 57 (4) (1995) 573–580. `doi:10.1016/0045-7949(95)00059-P`.

[44] B. Li, F. Habbal, M. Ortiz, Optimal transportation meshfree approximation schemes for fluid and plastic flows, International Journal for Numerical Methods in Engineering 83 (12) (2010) 1541–1579. `doi:10.1002/nme.2869`.
URL `http://doi.wiley.com/10.1002/nme.2869`